

## Supplementary Information

### **Bulk-Free Topological Insulator Bi<sub>2</sub>Se<sub>3</sub> nanoribbons with Magnetotransport Signatures of Dirac Surface States**

Gunta Kunakova<sup>1,2</sup>, Luca Galletti<sup>1</sup>, Sophie Charpentier<sup>1</sup>, Jana Andzane<sup>2</sup>, Donats Erts<sup>2</sup>,  
François Léonard<sup>3</sup>, Catalin D. Spataru<sup>3</sup>, Thilo Bauch<sup>1</sup> and Floriana Lombardi<sup>1</sup>

<sup>1</sup>*Quantum Device Physics Laboratory, Department of Microtechnology and Nanoscience,  
Chalmers University of Technology, SE-41296 Gothenburg, Sweden*

<sup>2</sup>*Institute of Chemical Physics, University of Latvia, Raina Blvd. 19, LV-1586,  
Riga, Latvia*

<sup>3</sup>*Sandia National Laboratories, Livermore, CA, 94551, United States*

## 1) Shubnikov-de Haas oscillations in Bi<sub>2</sub>Se<sub>3</sub> nanoribbons

### 1-1) Thin nanoribbons ( $t < 35\text{nm}$ )

In Fig. S1-a we show Shubnikov-de Haas (SdH) oscillations for three nanoribbons with thicknesses 26 – 31 nm. The Fast Fourier Transform (FFT) spectra give one dominating frequency ( $F$ ) around 100 T (Fig. S1-b). The determined frequency of SdH oscillations is used to calculate the 2D carrier density  $n_{2D,SdH} = k_F^2/4\pi = 2 \times 10^{12} \text{ cm}^{-2}$  (Table S1).

The cyclotron mass  $m_c$  is calculated in agreement with the Lifshitz – Kosevich theory. The  $\Delta R_{xx}$  values as a function of temperature at fixed magnetic field positions corresponding to the Landau Indices  $N = 7; 8; 9$  are shown in Fig. S2-a. The amplitude of the oscillations with the increase of the temperature can be expressed as  $\Delta R_{xx}(T) \propto (2\pi^2 k_B T / \hbar \omega) / (\sinh(2\pi^2 k_B T / \hbar \omega))$ , where  $k_B$  is the Boltzmann constant,  $\hbar$  is the reduced Planck constant,  $\omega$  is the cyclotron frequency<sup>1</sup>. By fitting the temperature dependent amplitude of the SdH oscillations in agreement with this equation, we extract  $\omega$ , which is then used to calculate the cyclotron mass as  $m_c = eB/\omega$ . The cyclotron mass is determined for 5 different magnetic field positions and the averaged  $m_c$  values are listed in the Table S1.

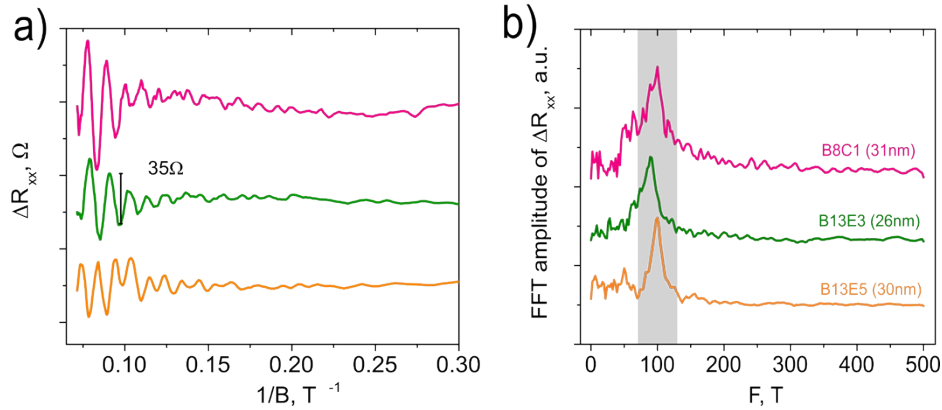


FIG. S1. a) Oscillatory part of the longitudinal magnetoresistance  $\Delta R_{xx}$  with removed background as a function of  $1/B$ . b) FFT amplitude of the  $\Delta R_{xx}$  for nanoribbons with thicknesses 26 – 31 nm.

To evaluate the 2D carrier mobility we performed a Dingle analysis (Fig. S2-b). Here we extracted the quantum lifetime  $\tau$  according to the relation  $\ln(\Delta R_{xx} B \sinh(\lambda(T))) \approx 1/B \times (2\pi^2 E_F / \tau e v_F^2)$ , where the thermal factor  $\lambda = 2\pi^2 k_B T m_c / eB$ . Extracted  $\tau$  was then used to calculate the 2D carrier mobility  $\mu_{SdH} = e\tau/m_c$ , where  $m_c$  is the cyclotron mass. Determined values of the  $\mu_{SdH}$  are given in Table S1.

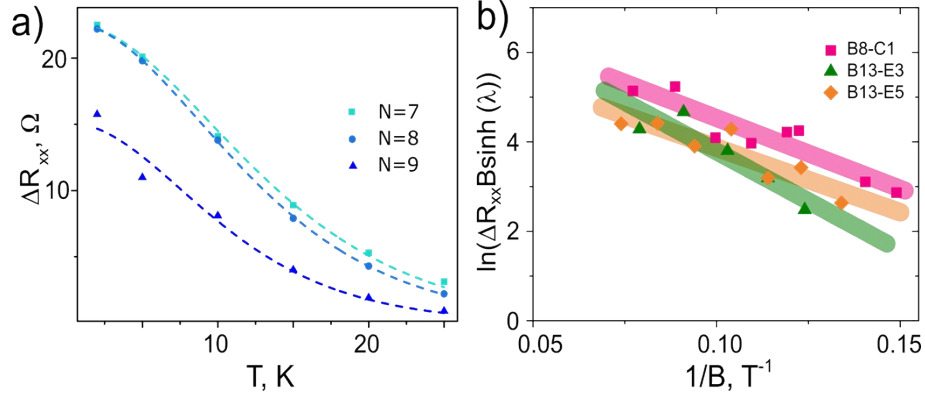


FIG. S2. a) Amplitude  $\Delta R_{xx}$  of the SdH oscillations as a function of temperature for nanoribbon B13-E3. The dashed curves correspond to the fit used to extract the cyclotron frequency.  $N = 7; 8; 9$  are assigned Landau indexes for several oscillation peaks. b) Dingle plots of three nanoribbons listed in Table S1. Solid – transparent lines are the fits used to extract the quantum lifetime and the corresponding 2D mobility.

TABLE S1. Summary of the calculated parameters from the SdH oscillations for the  $\text{Bi}_2\text{Se}_3$  nanoribbons.

No	Nanoribbon	$t$ , nm	$F$ , T	$n_{2D, \text{SdH}}$ , $\text{cm}^{-2}$	$\beta$	$\mu_{\text{SdH}}$ , $\text{cm}^2(\text{Vs})^{-1}$	$m_c / m_e$
1	B13-E3	26	88	$2.1 \times 10^{12}$	$0.48 \pm 0.03$	$4500 \pm 1100$	$0.145 \pm 0.021^*$
2	B13-E5	30	99	$2.4 \times 10^{12}$	$0.23 \pm 0.06$	$6800 \pm 1400$	*
3	B8-C1	31	96	$2.3 \times 10^{12}$	$0.22 \pm 0.03$	$6200 \pm 900$	$0.136 \pm 0.011$

\*The value of cyclotron mass of nanoribbon B13-E3 is used in the  $\mu_{\text{SdH}}$  calculations for nanoribbon B13-E5.

SdH oscillations for thin nanoribbons ( $t = 26 - 31$  nm) are represented by a single oscillation frequency. We can use these data to construct a Landau level fan diagrams for extracting a Berry phase (this is not the case for complicated multi-frequency SdH oscillation patterns, as observed for thicker nanoribbons, where reliable fan diagrams cannot be constructed due to overlapping of several frequencies). The Berry phase can be determined from a linear fit of Landau level fan diagram. Here the intercept  $\beta$  with the  $y$  axis relates with the Berry phase as  $\beta = \varphi/2\pi$ . For Dirac fermions, the Berry phase  $\varphi = \pi$  and the intercept  $\beta = 0.5$ .

A reliable Landau level fan diagram can be constructed considering both longitudinal and transversal components of the magnetotransport measurements, i.e., from conductivity tensor

$$\sigma_{xx} = \frac{\rho_{xx}}{\rho_{xx}^2 + \rho_{xy}^2}; \sigma_{xy} = -\frac{\rho_{xy}}{\rho_{xy}^2 + \rho_{xx}^2} \text{ and the Landau levels are indexed by taking the minima of } \sigma_{xx}^2.$$

Depending on  $\rho_{xx}$  and  $\rho_{xy}$  ratio, there are two different conditions <sup>2</sup>:

- 1)  $\sigma_{xx} \ll \sigma_{xy}$ ,  $\rho_{xx} \approx \sigma_{xx}/\sigma_{xy}^2$ ; *min* in  $\rho_{xx}$  is *min* in  $\sigma_{xx}$
- 2)  $\sigma_{xx} \gg \sigma_{xy}$ ,  $\rho_{xx} \approx 1/\sigma_{xx}$ ; *max* in  $\rho_{xx}$  is *min* in  $\sigma_{xx}$ .

By converting magnetoresistance data to conductivity tensor, we find that the  $\sigma_{xx} < \sigma_{xy}$  (see also Fig. 2b in the main text, where the conductance tensor data is plotted for the two-carrier analysis) and *min* in  $\rho_{xx}$  should coincide with *min* in  $\sigma_{xx}$ .

Fig. S3-a shows SdH oscillations for nanoribbon B13-E5, thickness – 30nm. Both  $\Delta\sigma_{xx}$  – tensor and plain  $\Delta\sigma_{xx}$  ( $=1/\rho_{xx}$ ) data with removed polynomial background are plotted. As expected for  $\sigma_{xx} < \sigma_{xy}$  condition, minima in  $\sigma_{xx}$  – tensor occur at the maxima of plain  $\sigma_{xx}$  (or at minima of  $\rho_{xx}$ ). The SdH oscillations in  $\sigma_{xx}$  – tensor have with a lower amplitude and are noisy compared to plain  $\sigma_{xx}$  due to the impact of low signal to noise  $R_{xy}$  data. Therefore, the best way to construct the Landau level diagrams for our  $\text{Bi}_2\text{Se}_3$  nanoribbons would be to index the minima in  $\rho_{xx}$ . The constructed Landau level fan diagrams with a linear fit for all three thin  $\text{Bi}_2\text{Se}_3$  nanoribbons are shown in Fig. S3-b. Extracted intercepts  $\beta = 0.22 - 0.48$  are summarized in Table S1.

To validate if the linear fitting in the Landau level fan diagrams is performed correctly, we plot the residual  $\Delta 1/B$  values from linear fit as a function of Landau indices  $N$ . As one can see, the residual of linear fit is scattered around zero for all three nanoribbons (Fig. S3-c).

The deviation from the value 0.5 for the extrapolated intercept expected for a linear Dirac dispersion is most probably caused by a parabolic contribution to the Dirac cone, which shifts the observed Berry phase extracted from SdH oscillation towards zero <sup>3</sup>. Such a parabolic contribution to the Dirac cone is consistently observed in ARPES measurements of  $\text{Bi}_2\text{Se}_3$  crystals.

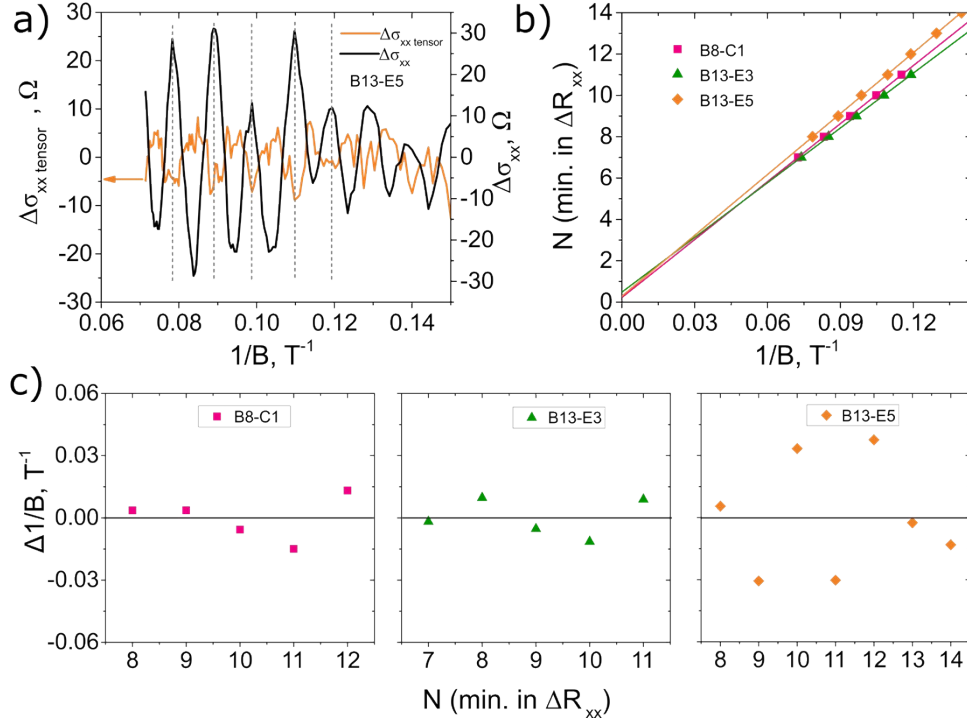


FIG. S3. Extraction of Berry phase for thin  $\text{Bi}_2\text{Se}_3$  nanoribbons. a)  $\sigma_{xx}$  – tensor and plain  $\sigma_{xx}(=1/\rho_{xx})$  data with removed polynomial background plotted as a function of  $1/B$ . b) Landau level diagrams of three nanoribbons listed in the Table S1. The solid lines are fit to extract the intercept with the  $y$  axis. c) Residual values of  $\Delta 1/B$  from linear fit of Landau level diagrams versus Landau indices  $N$  labelled to minima of  $\Delta R_{xx}$ .

The angular dependence of the SdH oscillations for thin nanoribbon (B8-C1) is plotted in Fig. S4. For a 2D surface, the oscillation frequency is expected to follow  $F \propto 1/\cos(\theta)$ , where  $\theta$  is the angle between the top surface of the nanoribbon and the field direction. The fact, that SdH oscillations align for all angles if plotting  $\Delta R_{xx}$  versus  $1/B \cos(\theta)$ , confirms the 2D nature of the SdH oscillations.

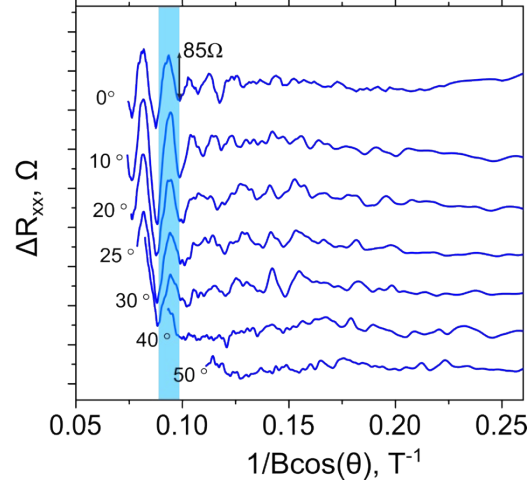


FIG. S4. SdH oscillations for the nanoribbon B8-C1 as a function of  $1/B \cos(\theta)$ . Angle at 0 deg represents magnetic field direction that is perpendicular to the nanoribbon top surface.

*1-2) Thick nanoribbons ( $t > 35\text{nm}$ )*

Thicker  $\text{Bi}_2\text{Se}_3$  nanoribbons (with thicknesses above 35nm) always shows multi-frequency SdH oscillation pattern. In Fig. S5 we plot the longitudinal magnetoresistance  $\Delta R_{xx}$  for 59 nm thick nanoribbon B21-B1, (extracted carrier densities for this nanoribbon are included in the main text, Table1). The FFT spectrum gives two dominating frequencies, which correspond to the surface and bulk carriers as discussed in the main text.

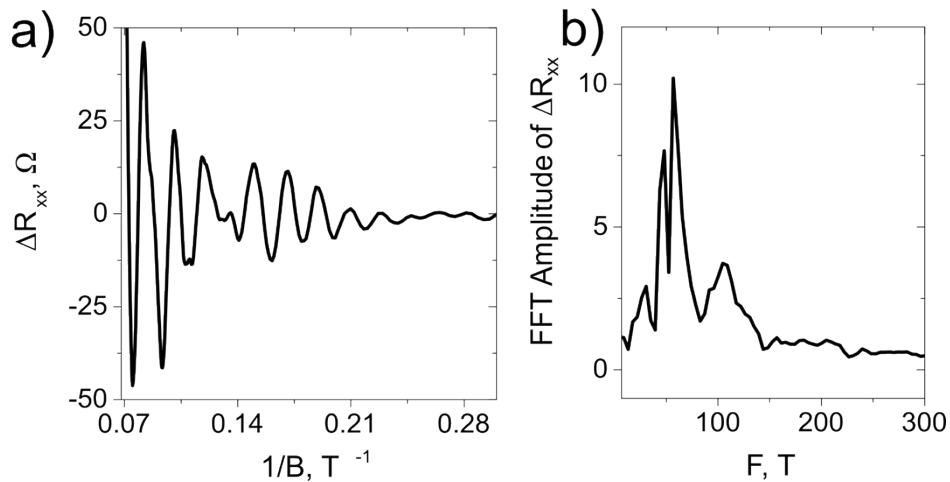


FIG. S5. a) Oscillatory part of the longitudinal magnetoresistance with removed smooth background  $\Delta R_{xx}$  as a function of  $1/B$ . b) FFT of the  $\Delta R_{xx}$ . Data correspond to nanoribbon B21-B1,  $t = 59\text{ nm}$ .

The FFT spectra of SdH oscillations for various magnetic field angles with respect to the surface normal for a thicker nanoribbon, shown in Fig. 4c of the main text, is depicted in Fig. S6.

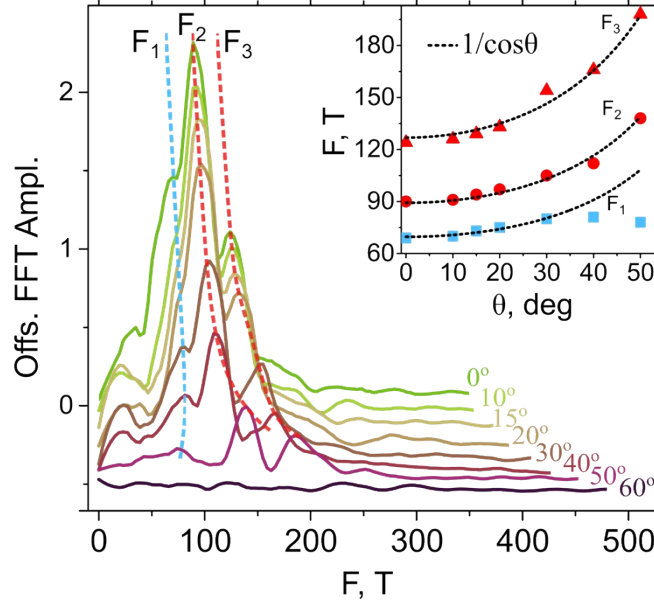


FIG. S6. FFT spectra of a thick TI nanoribbon ( $t = 57$  nm) for various angles of the applied magnetic field  $\theta$ , where  $\theta=0^\circ$  corresponds to a field applied perpendicular to the TI nanoribbon surface. The inset shows the evolution of the three main peaks as a function of angle  $\theta$ .

The FFT spectra of this nanoribbon gives three frequencies:  $F_1$ ,  $F_2$  and  $F_3$ . Two higher frequencies  $F_3 = 127$ T and  $F_2 = 90$ T follows  $1/\cos\theta$  dependence and they clearly originate from a 2D Fermi surface. These frequencies represent Dirac surface states at the nanoribbon top surface (see discussion in main text). The fact that there are two 2 oscillation frequencies with the  $1/\cos\theta$  dependence can be related to existing terrace in the nanoribbon top surface (see AFM image of this nanoribbon in Fig. S7). Corresponding 2D carrier density calculated from  $F_2$  and  $F_3$  is  $2.2$  and  $3 \times 10^{12} \text{cm}^{-2}$ , which is similar with those carrier density values extracted from a single-frequency SdH oscillations (see in Table S1).

The lowest  $F_1 = 70$ T shows deviation from  $1/\cos\theta$  dependence and is attributed to the bulk electrons. The bulk carrier density is calculated as  $n_{3D,SdH} = 1/(2\pi)^2(4/3) k_F^3$ , and  $n_{3D,SdH} = 3.3 \times 10^{18} \text{cm}^{-3}$ .

This value is in agreement with an expected ellipsoidal Fermi surface for the bulk <sup>4,5</sup>, resulting in a departure from the expected  $1/\cos\theta$  dependence of SdH oscillation frequency for a 2D Fermi surface or a 3D cylindrical Fermi surface (limit of large bulk carrier concentration  $10^{20} \text{cm}^{-3}$ ).

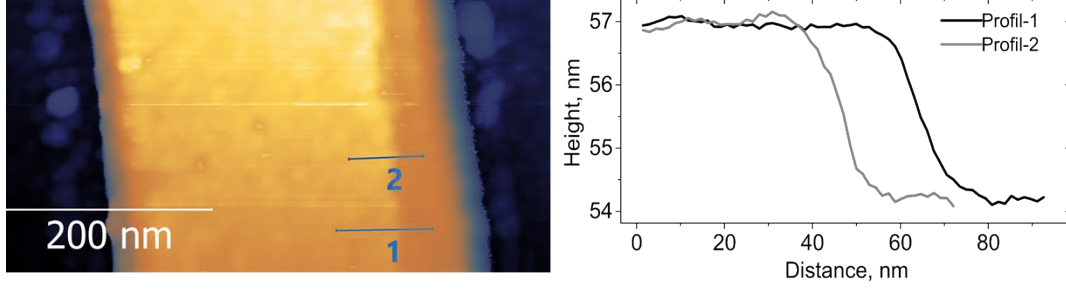


FIG. S7. Atomic Force Microscopy image of the  $\text{Bi}_2\text{Se}_3$  nanoribbon shown in Fig. S6. A step/terraces can be clearly observed in the nanoribbon surface. The right panel shows line scans indicated by the lines 1 and 2 in the left panel.

## 2) Hall effect in individual nanoribbons

To extract the total Hall carrier density (and to perform a two-carrier analysis as discussed in the main text), we have measured  $R_{xy}$  magnetoresistance at high magnetic field intensities up to 14 T.  $R_{xy}$  characteristics are nonlinear at magnetic field values above 2T. This fact confirms multi-band transport in our TI nanoribbons. The total Hall carrier density can be determined from the high-field region 12 – 14T. The determined values are about 20% higher compare to those extracted from 0-2T region. These data are shown in the main text, Fig. 1c.

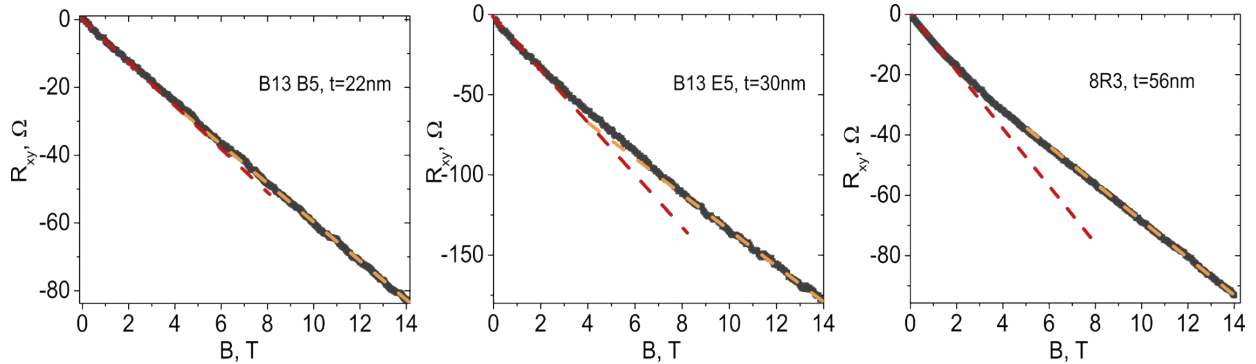


FIG. S8. Transversal resistance  $R_{xy}$  as a function of magnetic field for  $\text{Bi}_2\text{Se}_3$  nanoribbons with different thicknesses ( $T = 2\text{K}$ ).

## 3) Gate dependence of $R_{xx}$ in individual nanoribbons

Fig S9 depicts gate dependence of the longitudinal resistance  $R_{xx}$  at temperature of 2 K for nanoribbons with different thicknesses. The 3D TIs are ambipolar materials and the gate

dependence of the  $R_{xx}$  can give additional information about the charge neutrality point (CNP), which usually is observed at large negative voltages in case of  $\text{SiO}_2$  as a gate dielectric<sup>6,7</sup>.

The CNP can be reached for a thinner  $\text{Bi}_2\text{Se}_3$  nanoribbon. As shown in Fig. S9-a, the CNP of the top surface (more than tenfold increase of  $R_{xx}$ ) is reached at a back gate voltage of -70 V. The main reason for applying such high gate voltage is to compensate the accumulation layer at the TI interface with the substrate.

For the 65 nm thick nanoribbon we do not reach the CNP even for applied voltages of -90V (Fig. S9-b), which is compatible with the existence of bulk charge carriers in parallel with the surface states at the top TI surface and the accumulation layer at the TI interface with the substrate. The fact that in thick nanoribbons we have bulk carriers makes it close to impossible to reach the charge neutrality point at the TI top surface.

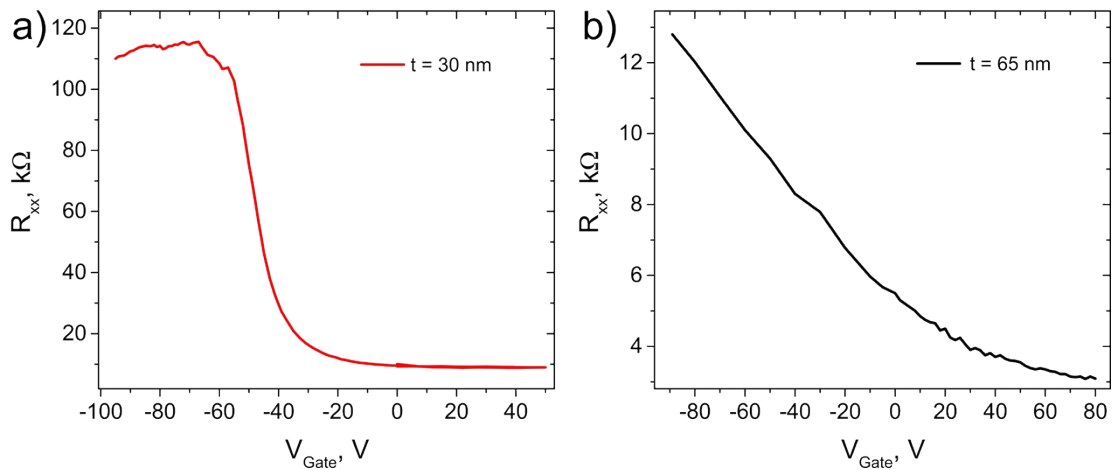


FIG. S9. Back - gate dependence of the longitudinal resistance at 2K for  $\text{Bi}_2\text{Se}_3$  nanoribbons: a)  $t = 30\text{nm}$  and b)  $t = 65\text{nm}$ .

#### 4) Band bending for $\text{Bi}_2\text{Se}_3$ nanoribbons

The band-bending diagrams for  $\text{Bi}_2\text{Se}_3$  nanoribbons are modelled by solving the Poisson's equation. For these simulations a self-consistent calculation for a slab of  $\text{Bi}_2\text{Se}_3$  with the boundary conditions set by the experimentally determined values of different carrier populations in  $\text{Bi}_2\text{Se}_3$  nanoribbons. Fig. S10 shows the simulated band-bending diagrams for thin  $\text{Bi}_2\text{Se}_3$  nanoribbons using this approach. The conduction band minimum (CBM) at distance "0 nm" (the "Dist." in the plots is the distance of  $\text{Bi}_2\text{Se}_3$  from the substrate) corresponds to the interface  $\text{Bi}_2\text{Se}_3/\text{SiO}_2$ , with

an accumulation layer. The CMB values at Dist.=0 nm are used to evaluate the band-bending energy at the interface  $\Delta E_{BB}^{Int}$  (Table 1, main text).

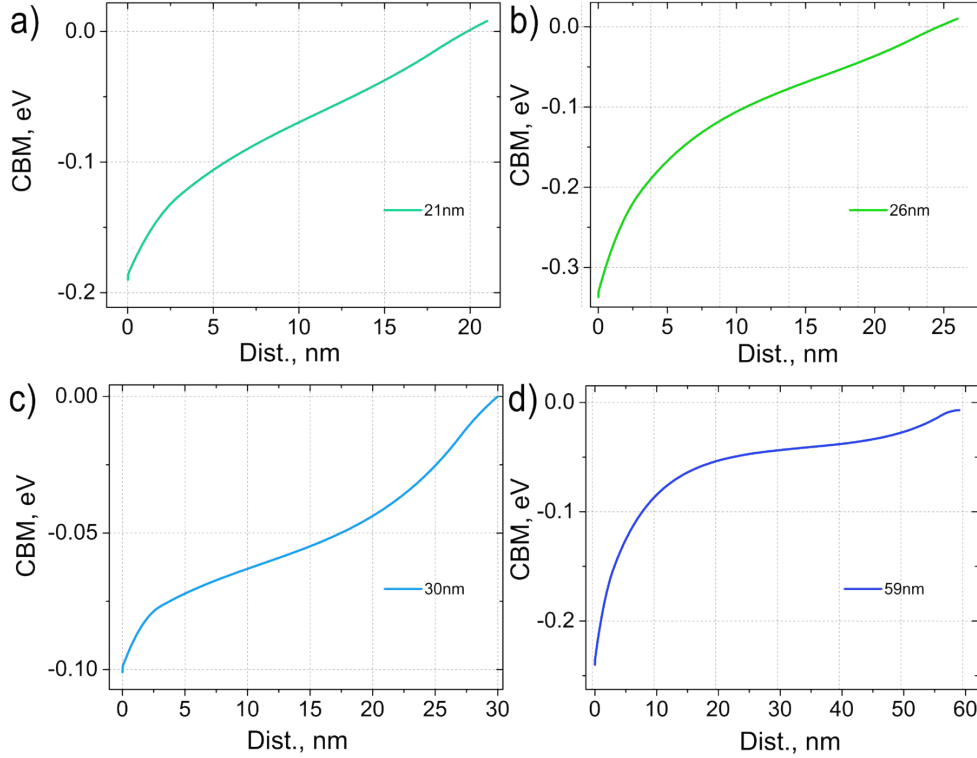


FIG. S10. a) – d) Band-bending diagrams for nanoribbons B13-C3 ( $t = 21$  nm); B13-E3 ( $t = 26$  nm); B13-E5 ( $t = 30$  nm) and B21-B1 ( $t = 59$  nm). The boundary conditions are set by the experimental values shown in the main text, Table 1. Dielectric constant used in the simulations  $\epsilon = 100$ .

## 5) Aharonov – Bohm oscillations

The longitudinal magnetoresistance of the  $\text{Bi}_2\text{Se}_3$  nanoribbon B8-C1 ( $t = 31$  nm,  $w = 260$  nm) as a function of *axial* magnetic field is shown in Fig. S11. The  $R_{xx}$  oscillates with the period of  $\Delta B = \Phi_0/A$ , where  $\Phi_0 = h/e$  is the magnetic flux quantum and  $A$  is the cross-section of a nanoribbon<sup>8</sup>.

The cross-section area is calculated as  $A = t \times w = 8.06 \times 10^{-15} \text{ m}^2$ . This value of cross-section would correspond to the oscillation period of 0.51 T, which is different than the experimentally observed  $\Delta B = 0.79$  T (Fig. S11). This discrepancy suggests, that the effective cross-section (the one representing the area where the charge transport takes place) is smaller than the geometrical. If we account for  $\sim 5$  nm thick layer of a native oxide commonly present on the

surfaces of  $\text{Bi}_2\text{Se}_3$  and  $\text{Bi}_2\text{Te}_3$ <sup>9</sup>, the cross-section area is  $5.25 \times 10^{-15} \text{ m}^2$  matching the experimentally determined  $\Delta B$  of 0.79 T.

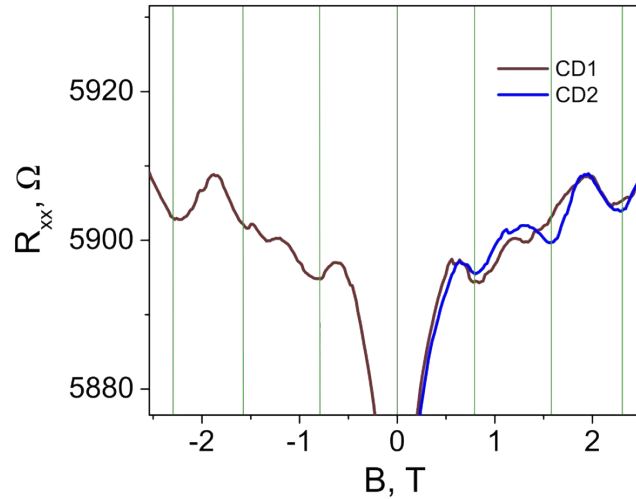


FIG. S11. Longitudinal resistance versus axial magnetic field. Data correspond to two thermal cycles CD1 and CD2 of the nanoribbon B8- C1 ( $t = 31 \text{ nm}$ ,  $w = 260 \text{ nm}$ ).

### 6) HR-TEM studies of the $\text{Bi}_2\text{Se}_3$ nanoribbons

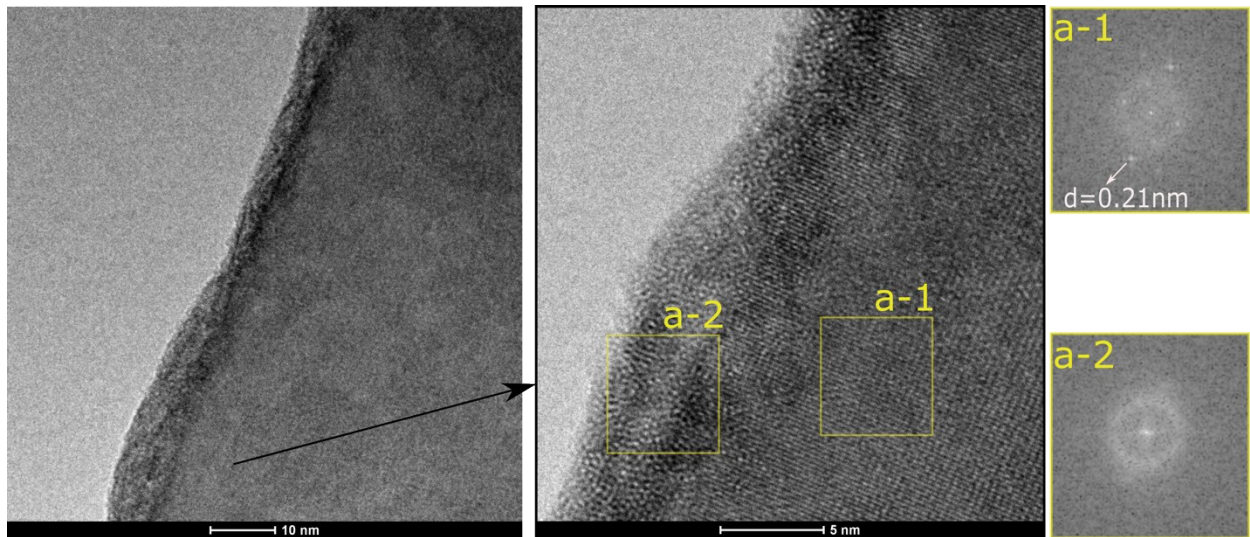


FIG. S12. High-resolution TEM images on a  $\text{Bi}_2\text{Se}_3$  nanoribbon

Fig. S12 illustrates HR-TEM studies of a  $\text{Bi}_2\text{Se}_3$  nanoribbon. The left panel provides an overview of a  $\text{Bi}_2\text{Se}_3$  nanoribbon, showing an oxide layer covering the nanoribbon surface. Close view of this oxide layer (of an average thickness of  $\sim 5 \text{ nm}$ ) and its interface with the single-

crystalline core of the nanoribbon is shown in higher magnification image (middle panel). The two panels on the right show FFT images corresponding to two different regions of the Bi<sub>2</sub>Se<sub>3</sub> nanoribbon, labelled a-1 and a-2. The FFT image corresponding to the a-1 area (the inner structure of the nanoribbon) shows a hexagonally symmetric pattern, confirming single-crystalline structure of Bi<sub>2</sub>Se<sub>3</sub>. The interplane spacing extracted from this pattern is ~0.21 nm, which is consistent with the interplane distance of [11 $\bar{2}$ 0] of Bi<sub>2</sub>Se<sub>3</sub><sup>10</sup>. The FFT image corresponding to the area a-2 (the surface layer of the nanoribbon) shows a ring indicating amorphous structure. The ring diameter approximately equates to a lattice spacing of 0.32 nm, meaning that the surface layer could correspond to a bismuth oxide<sup>11</sup> and/or selenium oxide<sup>12</sup> layer formed from air exposure.

## References:

- (1) Isihara, A.; Smrčka, L. Density and Magnetic Field Dependences of the Conductivity of Two-Dimensional Electron Systems. *J. Phys. C Solid State Phys.* **1986**, *19*, 6777–6789.
- (2) Ando, Y. Topological Insulator Materials. *J. Phys. Soc. Japan* **2013**, *82*, 102001–102032.
- (3) Taskin, A. A.; Ando, Y. Berry Phase of Nonideal Dirac Fermions in Topological Insulators. *Phys. Rev. B - Condens. Matter Mater. Phys.* **2011**, *84*, 1–6.
- (4) Lawson, B. J.; Li, G.; Yu, F.; Asaba, T.; Tinsman, C.; Gao, T.; Wang, W.; Hor, Y. S.; Li, L. Quantum Oscillations in Cu<sub>x</sub>Bi<sub>2</sub>Se<sub>3</sub> in High Magnetic Fields. *Phys. Rev. B* **2014**, *90*, 195141.
- (5) Lahoud, E.; Maniv, E.; Petrushevsky, M. S.; Naamneh, M.; Ribak, A.; Wiedmann, S.; Petaccia, L.; Salman, Z.; Chashka, K. B.; Dagan, Y.; *et al.* Evolution of the Fermi Surface of a Doped Topological Insulator with Carrier Concentration. *Phys. Rev. B* **2013**, *88*, 195107.
- (6) Checkelsky, J. G.; Hor, Y. S.; Cava, R. J.; Ong, N. P. Bulk Band Gap and Surface State Conduction Observed in Voltage-Tuned Crystals of the Topological Insulator Bi<sub>2</sub>Se<sub>3</sub>. *Phys. Rev. Lett.* **2011**, *106*, 196801.
- (7) Hong, S. S.; Cha, J. J.; Kong, D.; Cui, Y. Ultra-Low Carrier Concentration and Surface-Dominant Transport in Antimony-Doped Bi<sub>2</sub>Se<sub>3</sub> Topological Insulator Nanoribbons. *Nat. Commun.* **2012**, *3*, 757.
- (8) Peng, H.; Lai, K.; Kong, D.; Meister, S.; Chen, Y.; Qi, X.-L.; Zhang, S.-C.; Shen, Z.-X.; Cui, Y. Aharonov-Bohm Interference in Topological Insulator Nanoribbons. *Nat. Mater.* **2010**, *9*, 225–229.
- (9) Tian, M.; Ning, W.; Qu, Z.; Du, H.; Wang, J.; Zhang, Y. Dual Evidence of Surface Dirac States in Thin Cylindrical Topological Insulator Bi<sub>2</sub>Te<sub>3</sub> Nanowires. *Sci. Rep.* **2013**, *3*, 1212.
- (10) Liu, F.; Liu, M.; Liu, A.; Yang, C.; Chen, C.; Zhang, C.; Bi, D.; Man, B. The Effect of Temperature on Bi<sub>2</sub>Se<sub>3</sub> Nanostructures Synthesized via Chemical Vapor Deposition. *J. Mater. Sci. Mater. Electron.* **2015**, *26*, 3881–3886.

- (11) Friedensen, S.; Mlack, J. T.; Drndić, M. Materials Analysis and Focused Ion Beam Nanofabrication of Topological Insulator  $\text{Bi}_2\text{Se}_3$ . *Sci. Rep.* **2017**, *7*, 13466.
- (12) Zhao, Q.; Zhang, H. Z.; Xiang, B.; Luo, X. H.; Sun, X. C.; Yu, D. P. Fabrication and Microstructure Analysis of  $\text{SeO}_2$  Nanowires. *Appl. Phys. A Mater. Sci. Process.* **2004**, *79*, 2033–2036.